A generalised method to estimate the kinetics of fast Ca2+ currents from Ca2+ imaging experiments

Karima Ait Ouares, Nadia Jaafari, Marco Canepari

Journal of Neuroscience Methods, in press

A generalised method to estimate the kinetics of fast Ca^{2+} currents from Ca^{2+} imaging experiments

Karima Ait Ouares[a,b], **Nadia Jaafari**[a,b] and **Marco Canepari**[a,b,c]

[a] Laboratory for Interdisciplinary Physics, UMR 5588, Université Grenoble Alpes and CNRS, 38402 Saint Martin d'Hères, France.

[b] Laboratories of Excellence, Ion Channel Science and Therapeutics, France.

[c] Institut National de la Santé et Recherche Médicale (INSERM), France.

Address of the submitting and corresponding author

Marco Canepari, Laboratoire Interdisciplinaire de Physique (UMR 5588), Bat. E45, 140 avenue de la physique, Domaine univ., 38402 St Martin d'Hères cedex, France. Email: marco.canepari@univ-grenoble-alpes.fr

Number of figures: 7

Number of Tables: 2

Words in the abstract: 244

Type of article: Research

Author contributions

K.A-O, N.J. and M.C performed the experiments. M.C. designed the study, developed the method, analysed the data and wrote the paper.

Keywords:

Calcium currents

Calcium imaging

CA1 hippocampal pyramidal neuron

Purkinje neuron

Calcium binding proteins

HIGHLIGHTS

- Imaging Ca^{2+} fluorescence at high temporal resolution
- Estimate the kinetics of Ca^{2+} currents
- Study the physiological function of neuronal Ca^{2+} channels

ABSTRACT

Background: Fast Ca^{2+} imaging using low-affinity fluorescent indicators allows tracking Ca^{2+} neuronal influx at high temporal resolution. In some systems, where the Ca^{2+}-bound indicator is linear with Ca^{2+} entering the cell, the Ca^{2+} current has same kinetics of the fluorescence time derivative. In other systems, like cerebellar Purkinje neuron dendrites, the time derivative strategy fails since fluorescence kinetics is affected by Ca^{2+} binding proteins sequestering Ca^{2+} from the indicator.

New Method: Our novel method estimates the kinetics of the Ca^{2+} current in cells where the time course of fluorescence is not linear with Ca^{2+} influx. The method is based on a two-buffer and two-indicator model, with three free parameters, where Ca^{2+} sequestration from the indicator is mimicked by Ca^{2+}-binding to the slower buffer. We developed a semi-automatic protocol to optimise the free parameters and the kinetics of the input current to match the experimental fluorescence change with the simulated curve of the Ca^{2+}-bound indicator.

Results: We show that the optimised input current is a good estimate of the real Ca^{2+} current by validating the method both using computer simulations and data from real neurons. We report the first estimates of Ca^{2+} currents associated with climbing fibre excitatory postsynaptic potentials in Purkinje neurons.

Comparison with Existing Methods: The present method extends the possibility of studying Ca^{2+} currents in systems where the existing time derivative approach fails.

Conclusions: The information available from our technique allows investigating the physiological behaviour of Ca^{2+} channels under all possible conditions.

1. Introduction

The possibility of measuring the kinetics of Ca^{2+} currents from fluorescence transients of a Ca^{2+} indicator allows studying the local activation and de-activation of Ca^{2+} channels during physiological activity. The founding principle of this measurement is that the fractional change of Ca^{2+} fluorescence ($\Delta F/F_0$) following a trans-membrane Ca^{2+} influx is proportional to the Ca^{2+} bound to the indicator if the dye-Ca^{2+} binding reaction has reached its equilibrium and if the indicator is not saturated (Sabatini and Regehr, 1998). Under this condition, the $\Delta F/F_0$ signal will be proportional to the integral of the Ca^{2+} current if two further conditions are met: (*A*) that the dye-Ca^{2+} binding reaction equilibration is faster than the kinetics of the Ca^{2+} current; and (*B*) that the Ca^{2+} binding reactions with the endogenous molecules of the cell are either also faster than the kinetics of the Ca^{2+} current or slower but negligible with respect to the dye-Ca^{2+} binding reaction during the time-window of the measurement.

We have previously demonstrated that both conditions are fulfilled by the Ca^{2+} indicator Oregon Green BAPTA-5N (OG5N) in the case of dendritic Ca^{2+} currents associated with back-propagating action potentials in CA1 hippocampal pyramidal neurons (Jaafari et al. 2014; 2015). OG5N is a low-affinity indicator (K_D = 35 µM, Canepari and Ogden, 2006) that equilibrates in <200 µs according to the Kao and Tsien theoretical estimate of the relaxation time (Kao and Tsien, 1988). Its ability to track the kinetics of voltage-gated Ca^{2+} channels (VGCCs) can be therefore considered universal in all cellular systems. The second condition, i.e. the linearity with the endogenous Ca^{2+} binding reactions, is however not universal. In the dendrites of CA1 hippocampal pyramidal neurons, where the endogenous buffer capacity (Canepari et al., 2008) is relatively low (~100, Helmchen et al., 1996; Maravall et al., 2000), the Ca^{2+}-$\Delta F/F_0$ signal associated with an action potential is essentially constant for the first 10 ms after the peak and decays only later in ~100 ms. Fig. 1A shows a representative example of dendritic Ca^{2+} transient associated with a back-propagating action potential from a cell filled with 2 mM OG5N. The $\Delta F/F_0$ signal starts rising near the peak of the action potential reaching a plateau for a few milliseconds after the end of the action potential. The flat behaviour of the $\Delta F/F_0$ signal after the end of the current indicates that not only the dye-Ca^{2+} binding, but also the Ca^{2+} binding to the endogenous buffer, have reached the equilibrium during this short time window (Jaafari et al., 2014). Hence, the time derivative of the $\Delta F/F_0$ signal has the same kinetics of the Ca^{2+} current. The CA1 hippocampal pyramidal neuron of Fig. 1B was filled with 2 mM OG5N and 100 µM BAPTA, a high-affinity Ca^{2+} buffer (K_D = 160 nM, Pethig et al., 1989). In contrast to the OG5N-Ca^{2+} binding reaction, the BAPTA-Ca^{2+} binding reaction equilibrates in the millisecond range. As BAPTA sequestrates Ca^{2+} from OG5N, the slope of the $\Delta F/F_0$ signal becomes negative after the end of the current deviating from the linear behaviour with the Ca^{2+} influx. In this case, the time derivative of the OG5N-$\Delta F/F_0$ signal does not match the kinetics of the Ca^{2+} current. Fig. 1C shows an example of dendritic Ca^{2+} transient associated with a climbing fibre excitatory postsynaptic potential (EPSP) from a cerebellar Purkinje neuron (PN) filled with 2 mM OG5N. In this cell type, where the endogenous buffer capacity is high (~2000, Fierro and Llano, 1996), the dendritic Ca^{2+}-$\Delta F/F_0$ signal associated with climbing fibre EPSPs decays more rapidly (Miyakawa et al., 1992) following the Ca^{2+} binding to slow endogenous buffers. Thus, the OG5N-$\Delta F/F_0$ time derivative in Fig. 1C has a negative component and does not reproduce the kinetics

of the Ca^{2+} current. Since the theoretical ability of Ca^{2+} imaging experiments for tracking a fast Ca^{2+} influx depends exclusively on the equilibration time of the indicator, a way to extract the kinetics of the Ca^{2+} current can be still developed if the kinetics of Ca^{2+} sequestration is taken into account. This is clearly a difficult task since the kinetics of Ca^{2+} binding proteins, measured with flash photolysis techniques (Faas and Mody, 2012), is very complex and depends on many parameters that vary from cell to cell. In contrast, a useful method should utilise a simple model with only a small number of degrees of freedom, allowing the development of a semi-automatic procedure to standardise the extraction of the Ca^{2+} current kinetics. In this report, we present a novel method to estimate the kinetics of the Ca^{2+} current based on this principle. The method applies a simple two-buffer and two-indicator model to the hypothetical current input to match the experimental time course of the OG5N-$\Delta F/F_0$ signal. The parameters of the model are set, initially, using the rising phase of the OG5N-$\Delta F/F_0$ time derivative as initial approximation of the current. The full kinetics of the current is then extrapolated by maximising the similarity between the experimental OG5N-$\Delta F/F_0$ signal and the equivalent curve obtained by computer simulation. To validate the method, we used combined fluorescence measurements from OG5N and Fura-2. In particular, since the time scale of Fura-2 equilibration is similar to that of endogenous Ca^{2+} binding proteins (Kao and Tsien, 1988), the measurement of Fura-2 $\Delta F/F_0$ (Fura-$\Delta F/F_0$) signal provided a direct estimate of Ca^{2+} sequestration. The usefulness and limitations of the estimate of the Ca^{2+} current kinetics, obtained with this approach, are discussed at the end of the paper.

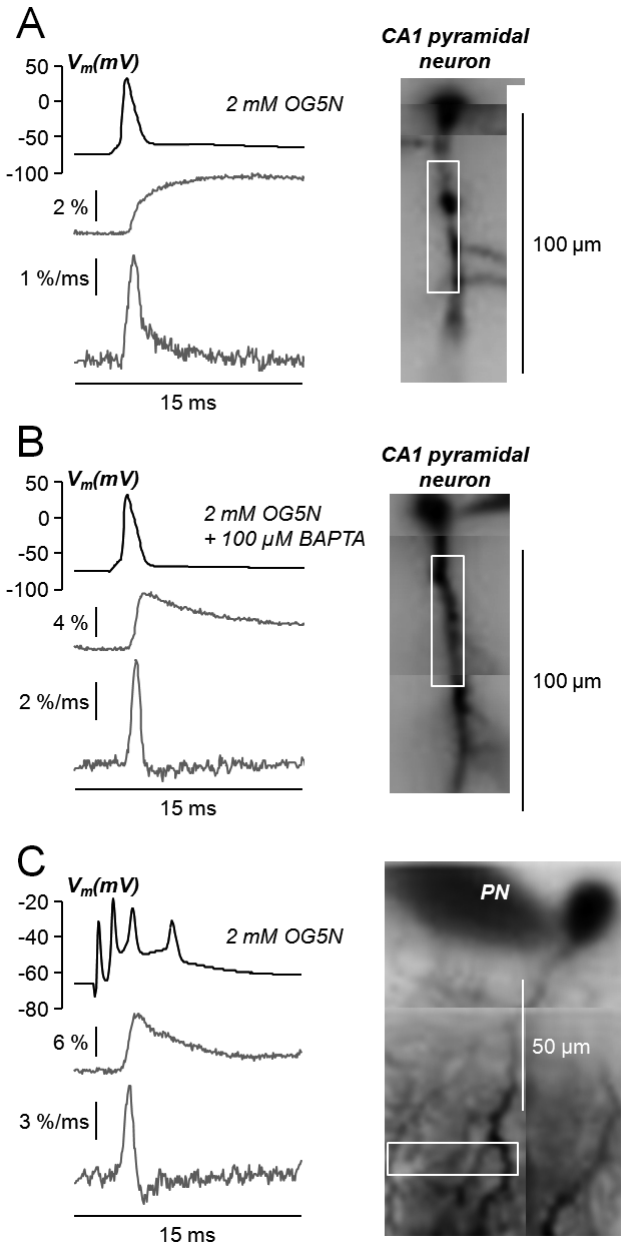

Fig. 1. *OG5N-$\Delta F/F_0$ signals in CA1 hippocampal pyramidal neurons and in PNs.* (A) OG5N-$\Delta F/F_0$ signal (2nd trace from the top) and its time derivative (3rd trace from the top) associated with an action potential (top trace) from the dendritic region of a CA1 hippocampal pyramidal neuron indicated on the right. The cell was filled with 2 mM OG5N. (B) same as A but in another CA1 hippocampal pyramidal neuron filled with 2 mM OG5N and 100 µM BAPTA. (C) OG5N-$\Delta F/F_0$ signal (2nd trace from the top) and its time derivative (3rd trace from the top) associated with a climbing fibre EPSP (top trace) from the dendritic region of a PN indicated on the right. The cell was filled with 2 mM OG5N. All data, recorded at 20 kHz, were from averages of 16 trials.

2. Materials and Methods

2.1 Slice preparation, solutions and electrophysiology

Experiments, performed at the Laboratoire Interdisciplinaire de Physique, were approved by the Isere prefecture (Authorisation n. 38 12 01). Transversal hippocampal slices and sagittal cerebellar slices (250 µm thick) were prepared from 24-35 postnatal days old C57Bl6 mice following published procedures (Vogt et al., 2011a; 2011b) using a Leica VT1200 (Leica, Wetzlar, Germany). Slices were cut in iced extracellular solution and incubated at 37°C for 1 hr before use. The extracellular solution contained (in mM): 125 NaCl, 26 $NaHCO_3$, 1 $MgSO_4$, 3 KCl, 1 NaH_2PO_4, 2 $CaCl_2$ and 20 glucose, bubbled with 95% O_2 and 5% CO_2. The intracellullar solution contained (in mM): 125 $KMeSO_4$, 5 KCl, 8 $MgSO_4$, 5 Na_2-ATP, 0.3 Tris-GTP, 12 Tris-Phosphocreatine, 20 HEPES, adjusted to pH 7.35 with KOH. The Ca^{2+} indicator Oregon Green 488 BAPTA-5N (OG5N, Invitrogen, Carlsbad, CA) was added at the concentration of 2 mM. In some experiments, the Ca^{2+} indicator Fura-2 (Invitrogen) was added at 400 µM. Chemicals were purchased from Sigma-Aldrich (St. Louis, MO). Experiments were performed at 32-34°C using an Olympus BX51 microscope equipped with a 60X/1.0 NA Nikon objective. Patch-clamp recordings were made using a Multiclamp amplifier 700A (Molecular Devices, Sunnyvale, CA) and recorded with the A/D board of the CCD camera. The membrane potential, measured with the patch pipette, was corrected for the junction potential (-11 mV) as previously estimated (Canepari et al., 2010). In PNs, climbing fibre EPSPs were elicited by current pulses, of 5-20 µA amplitude and 100 µs duration, which were delivered by a pipette placed in granule cell layer near the recording cell. In CA1 hippocampal pyramidal neurons, somatic action potentials were elicited by 2 ms depolarising current injections through the patch pipette.

2.2 Optical recordings and analysis

OG5N and Fura-2 fluorescence were excited at 470 nm and 385 nm respectively with an OptoLED (CAIRN Research Ltd., Faversham, UK). Both fluorescence signals, filtered at 510 ± 42 nm, were recorded using a NeuroCCD-SMQ camera (RedShirtimaging, Decatur, GA). Images, de-magnified by ~0.25X to visualise ~150 µm, were acquired at 5 kHz with a resolution of 26 X 26 pixels, except in the case of Fig 1 in which the sampling frequency was 20 kHz and the resolution of 26 X 4. All recordings were performed at least 35 minutes after establishing the whole cell configuration to allow equilibration of the indicators. To average multiple trials, consistency was verified by checking the somatic electrical signal. Fluorescence averages were corrected for bleaching using filtered trials without signal. All data were analysed with Matlab (The Mathworks, Natick, MA). $\Delta F/F_0$ signals were calculated after subtraction of the autofluorescence background.

2.3 Models and simulations

A general model for Ca^{2+} dynamics in a cell cytoplasm after an influx is illustrated in Fig. 2A and described by the set of 2N +1 equations:

$$\frac{d[Ca^{2+}]}{dt} = \xi_{Ca} - \sum_{j=1}^{N} (K_{ON}^{B_j} \cdot [B_j] \cdot [Ca^{2+}] - K_{OFF}^{B_j} \cdot [B_j Ca^{2+}]) - \varepsilon \cdot \frac{[Ca^{2+}]}{[Ca^{2+}] + \theta_M}$$

$$\frac{d[B_j Ca^{2+}]}{dt} = K_{ON}^{B_j} \cdot [Ca^{2+}] \cdot [B_j] - K_{OFF}^{B_j} \cdot [B_F Ca^{2+}]$$

$$\frac{d[B_j]}{dt} = -\frac{d[B_j Ca^{2+}]}{dt}$$

This model comprises N buffers, with association and dissociation constants K_{ON}^{Bj} and K_{OFF}^{Bj} respectively, which represent the different binding sites of Ca^{2+} binding proteins and possibly to exogenous Ca^{2+} chelators such as the indicators. The model also includes Ca^{2+} extrusion with Michaelis-Menten kinetics, where ε is a factor that depends on the pumps velocity and θ_M is the Michaelis-Menten constant. The input ξ_{Ca} is the Ca^{2+} current to volume ratio, i.e. the curve that we are aiming at estimating. A simplified version of the general model is the two-buffer model (Nowycky and Pinter, 1993; Canepari and Mammano, 1999). Here, as shown in Fig. 2B, the two buffers are a fast buffer (B_F) and a slow buffer (B_S). The presence of a fast dye (D_F), representing OG5N, and possibly of a slow dye (DS), representing Fura-2, complete the simplified model leading to nine or seven differential equations, depending on whether or not Fura-2 is added in the experiment. We used this simplified model to fit the experimental OG5N-$\Delta F/F_0$ signal with the $[D_F Ca^{2+}]$ resulting from computer simulations using the function "ode45" in Matlab. In all simulations, the ξ_{Ca} input was expressed as sum of four Gaussian functions:

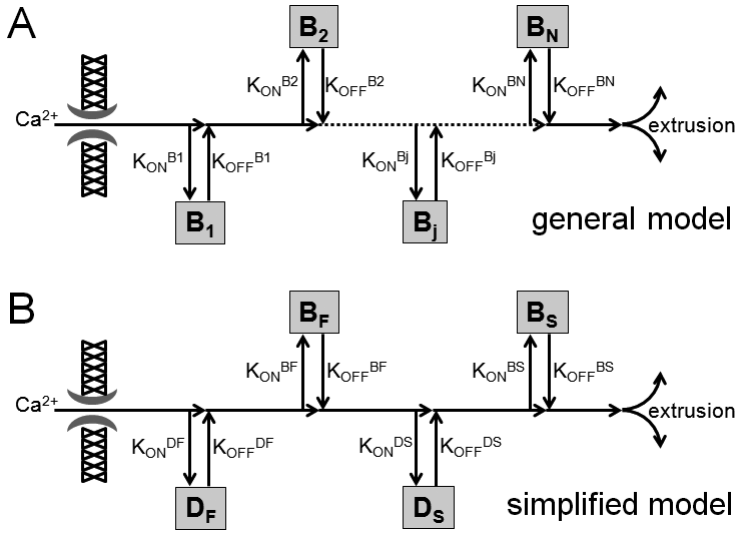

Fig. 2. *Models of cellular Ca^{2+} binding kinetics.* (A) General model of Ca^{2+} cellular influx and reaction with N buffers followed by extrusion. (B) Simplified version of the model in A, used in our method, with a fast and a slow endogenous buffer (B_F and B_S) and with a fast and a slow Ca^{2+} indicator (D_F and D_S).

$$\xi_{Ca}(t) = \sum_{k=1}^{4} \xi_{Ca}^{k} \cdot e^{-\left(\frac{t-\alpha k}{\beta k}\right)^2}$$

For both dyes, the diffusion-limited association constant (K_{ON}^{DF} and K_{ON}^{DS}) was set to 570· $\mu M^{-1}s^{-1}$ as in a previous study (Canepari and Mammano, 1999), the total concentrations were those of the patch pipette and the equilibrium constant ($K_D = K_{OFF}/K_{ON}$) was set to 35 μM for OG5N (Canepari and Ogden, 2006) and 0.24 μM for Fura-2 (Shuttleworth and Thompson, 1991). We arbitrarily set the equilibrium constants of the fast and slow buffers to 10 μM and 0.2 μM respectively, and the association constant of the fast buffer (K_{ON}^{BF}) equal to that of the dyes. The concentrations of the fast and slow buffers and the association constant of the slow buffer were varied to optimise the similarity between the experimental OG5N-$\Delta F/F_0$ signal and the simulated $[D_F Ca^{2+}]$. Finally, the extrusion constants ε and and θ_M were set to 1000 $\mu M \cdot s^{-1}$

and 3 µM respectively. To fit experimental data, we associated the Ca^{2+}-bound concentrations of OG5N and Fura-2 ($[D_FCa^{2+}]$ and $[D_SCa^{2+}]$) with their respective fluorescence (F) signals using the two equations:

$$\left[D_FCa^{2+}\right] = [D_F]_{TOT} \cdot \frac{F^{DF} - F^{DF}_{zero}}{F^{DF}_{sat} - F^{DF}_{zero}}$$

$$\left[D_SCa^{2+}\right] = [D_S]_{TOT} \cdot \frac{F^{DS} - F^{DS}_{zero}}{F^{DS}_{sat} - F^{DS}_{zero}}$$

Where F_{zero} and F_{sat} are the fluorescence values at zero and saturating Ca^{2+} respectively and $[D_F]_{TOT}$ and $[D_S]_{TOT}$ are the total concentrations of OG5N (2 mM) and Fura (400 µM) respectively. Assuming the initial fluorescence (F_0) equal to F_{zero}, the variable $[D_FCa^{2+}]$ and $[D_SCa^{2+}]$ can be obtained from the OG5N-$\Delta F/F_0$ signal and the $\Delta F/F_0$ signal from Fura-2 (Fura-$\Delta F/F_0$) by using the two equations:

$$\left[D_FCa^{2+}\right] = [D_F]_{TOT} \cdot \frac{OG5N\text{-}\Delta F/F_0}{\sigma^{DF}}$$

$$\left[D_SCa^{2+}\right] = [D_S]_{TOT} \cdot \frac{Fura\text{-}\Delta F/F_0}{\sigma^{DS}}$$

where σ^{DF} and σ^{DS} are the *dynamic range factors* defined as $(F_{sat} - F_0)/F_0$. To measure σ^{DF} and σ^{DS}, we filled 9 CA1 pyramidal neurons with 0.5 mM OG5N and, 4 of them, also with 0.1 mM Fura-2. In these cells, in the presence of 4 mM extracellular $CaCl_2$, the somatic membrane was made permeable to Ca^{2+} by applying a 30s step of – 500 mV in voltage clamp, is this way saturating the indicators. σ^{DF}, which did not depend on the presence of Fura-2 concentration, was globally 15 ± 2 (N = 9 cells). σ^{DS} was -0.44 ± 0.07 (N = 4 cells). The simulation of $[D_FCa^{2+}]$ was divided by the mean value of $\sigma^{DF}(15)$ to match the corresponding experimental $\Delta F/F_0$ signal. The simulation of $[D_SCa^{2+}]$ was divided by a value ranging between -0.37 to -0.48 value to match the corresponding experimental $\Delta F/F_0$ signal.

2.4 Quantification of the similarity between two curves

To quantify the similarity between the curves from computer simulations and the experimental $\Delta F/F_0$ signals, we found that the simple comparison of the signals gave ambiguous results. We therefore used a classical approach based on the estimate of the correlation between the two curves in the frequency (v) domain. In detail, defining ΔG as $\sigma \cdot [DCa^{2+}]/[D]_{TOT}$, where D is the dye (either OG5N or Fura-2) and σ its dynamic range factor, the similarity between ΔG and $\Delta F/F_0$ was estimated by calculating their *magnitude squared coherence* $\Gamma_{\Delta F/F0}$:

$$\Gamma_{\Delta F/F0}(v) = \frac{|\Pi_{\Delta F\Delta G}(v)|^2}{\Pi_{\Delta F\Delta F}(v) \cdot \Pi_{\Delta G\Delta G}(v)}$$

where $\Pi_{\Delta F\Delta F}(v)$ and $\Pi_{\Delta G\Delta G}(v)$ are the *power spectral densities* of $\Delta F/F_0$ (ΔF in the equations below) and ΔG respectively, and $\Pi_{\Delta F\Delta G}(v)$ is their *cross power spectral density*. $\Gamma_{\Delta F/F0}(v)$ is the fractional part of ΔG that matches ΔF at the frequency v and, therefore, $\Gamma_{\Delta F/F0}(\underline{v}) = 1$ if ΔF and ΔG are identical at $v = \underline{v}$. The frequency functions $\Pi_{\Delta F\Delta F}(v)$, $\Pi_{\Delta G\Delta G}(v)$ and $\Pi_{\Delta F\Delta G}(v)$ (see for example Oppenheim and Schafer, 1999) are normally computed with the equations:

$$\Pi_{\Delta F\Delta F}(v) = \frac{\Delta t}{N} \cdot \left| \sum_{k=1}^{N} \Delta F_k \cdot e^{-ivk} \right|^2$$

$$\Pi_{\Delta G\Delta G}(v) = \frac{\Delta t}{N} \cdot \left| \sum_{k=1}^{N} \Delta G_k \cdot e^{-ivk} \right|^2$$

$$\Pi_{\Delta F\Delta G}(v) = \frac{\Delta t}{N} \cdot \sum_{k=1}^{N} \left(\sum_{h=1}^{N} \Delta F_h \cdot \Delta G_{h+k} \right) \cdot e^{-ivk}$$

where Δt is sampling time and N is the number of samples. In our method, however, we found convenient to calculate $\Gamma_{\Delta F/F0}$ in Matlab (Signal Processing Toolbox) using the function “mscohere” that uses the Welch's averaged modified periodogram method (Welch, 1967) to compute $\Pi_{\Delta F\Delta F}(v)$, $\Pi_{\Delta G\Delta G}(v)$ and $\Pi_{\Delta F\Delta G}(v)$ with minimal effect of the noise. In particular, since the precise frequency information is irrelevant for the purpose of our method, the segments used for the calculation of Welch $\Gamma_{\Delta F/F0}$ were windowed with a two-point *Hamming window* to obtain a nearly uniform $\Gamma_{\Delta F/F0}$ over v range of 0 – 1 kHz. This quantification was found efficient as $\Gamma_{\Delta F/F0}$ approached 1 when the curve from computer simulation matched the experimental $\Delta F/F_0$ signal. Thus, in the optimisation protocol described in the results, the parameters of the current input and of the models were set to maximise the mean $\Gamma_{\Delta F/F0}$ over the range $0 < v < 1$ kHz ($<\Gamma_{\Delta F/F0}>$). Empirically, we considered the optimisation process satisfactory if $<\Gamma_{\Delta F/F0}>$ was > 0.96.

3. Results

3.1 Limitations of extracting the Ca^{2+} current kinetics by using a simple time derivative

The method of extracting the Ca^{2+} current kinetics by calculating the time derivative of the OG5N-$\Delta F/F_0$ signal is based on the assumption that the kinetics of the OG5N-Ca^{2+} binding reaction is linear with the kinetics of Ca^{2+} binding to the endogenous buffers. This assumption is realistic if the slope of the $\Delta F/F_0$ signal is zero after the end of the current for a time window as long as the duration of the current (Canepari et al., 2014). If a buffer with higher affinity but slower equilibrium constant with respect to OG5N is present, this will sequestrate Ca^{2+} from OG5N producing an early decay phase and a negative component in the OG5N-$\Delta F/F_0$ time derivative. To illustrate this general concept, we show in Fig. 3 the results of computer simulations from a two-buffer model at increasing slow buffer concentrations. The model includes a realistic slow extrusion mechanism which is capable of re-establishing the initial Ca^{2+} conditions, as described in Materials and Methods. To visualise the difference between the real current and the time derivative of the $\Delta F/F_0$ signal, we used two input currents illustrated in Fig. 3(A). The first current on the left is a simple Gaussian function with a time constant of 0.5 ms. The second current on the right is the summation of the same fast current plus a smaller and slower current which is also a Gaussian function. Fig. 3(B) (top) shows the OG5N-$\Delta F/F_0$ signals in simulations where the cell has only 1 mM of a fast buffer with K_D = 10 μM. The traces on the bottom show the kinetics of the time derivative of the OG5N-$\Delta F/F_0$ signal. In this case, as expected, the time derivatives of the OG5N-$\Delta F/F_0$ signal and the input currents have the same kinetics. Thus, the slow decay of the OG5N-$\Delta F/F_0$ signals produced by the Ca^{2+} extrusion has negligible effect on the time derivatives of the OG5N-$\Delta F/F_0$ signal and does not produce

negative components in its time derivative. Fig. 3(C) and Fig. 3(D) (top traces) show the OG5N-$\Delta F/F_0$ signals in two simulations where the model includes an additional slow buffer with K_{ON} = 200 $\mu M^{-1}s^{-1}$ and K_D = 0.2 µM at concentrations of 100 and 400 µM respectively. In these cases, the faster decay of the OG5N-$\Delta F/F_0$ signal results in a difference between the time derivative of the OG5N-$\Delta F/F_0$ signal and the input current. This difference is however minimal for the rising phase of the fast current. Therefore, the time derivative of the OG5N-$\Delta F/F_0$ signal can be still considered an approximation of the real current in its initial phase. The goal is to develop a strategy to obtain a curve that approaches the kinetics of the real current, starting from the time derivative of the OG5N-$\Delta F/F_0$ signal as first approximation. This is done by optimising the parameters of a simplified kinetic model to reach a simulated OG5N-$\Delta F/F_0$ signal matching the experimental one. The parameters are determined by those characteristics of the experimental signal that depend only weakly on the full kinetics of the current input.

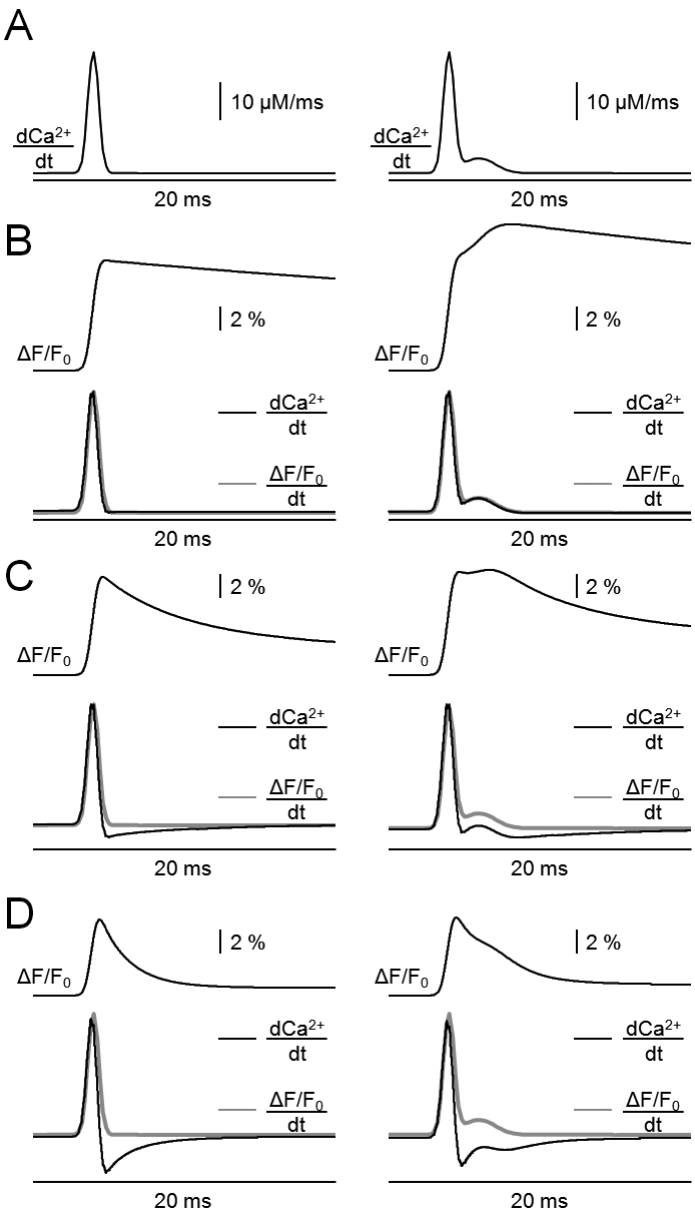

Fig. 3. *Theoretical examples of distortions of Ca^{2+} currents calculated as OG5N-$\Delta F/F_0$ time derivative.* (A) Model Ca^{2+} currents used for computer simulations. Left: dCa^{2+}/dt = (40 µM/ms)·exp(-[(t-4ms)/0.5ms)]^2). Right: dCa^{2+}/dt = (40 µM/ms)·exp(-[(t-4ms)/0.5ms)]^2) + (5 µM/ms)·exp(-[(t-6ms)/1.5ms)]^2). (B) Results of computer simulations of OG5N (2 mM) kinetics with 1 mM of a fast buffer with K_D = 10 µM; the black traces are the expected $\Delta F/F_0$ signal (top) and its time derivative (bottom); the superimposed bottom greytraces are the input Ca^{2+} currents reported in panel A. (C) Same as B with additional 100 µM of a slow buffer with K_D = 0.2 µM. (D) Same as B with additional 400 µM of a slow buffer with K_D = 0.2 µM.

3.2 Correcting the time derivative to account for a slow buffer using a semi-automatic protocol

To address the problem introduced at the end of the previous paragraph we used computer simulations corresponding to three more complex scenarios that may occur in real cells. In detail, we produce three "experimental" OG5N-$\Delta F/F_0$ signals from models that comprise four progressively slower and stronger buffers: a low-affinity buffer (K_{ON} = 570 $\mu M^{-1}s^{-1}$ and K_D = 10 µM); a medium-affinity buffer (K_{ON} = 570 $\mu M^{-1}s^{-1}$ and K_D = 1 µM); a fast high-affinity buffer (K_{ON} = 400 $\mu M^{-1}s^{-1}$ and K_D = 0.4 µM); and a slow and high-affinity buffer (K_{ON} = 200 $\mu M^{-1}s^{-1}$ and K_D = 0.1 µM); The parameters of the three particular scenarios are reported in Table 1. In the first scenario, the model contains 250 µM of the low-affinity buffer and 100 µM of each high-affinity buffer.

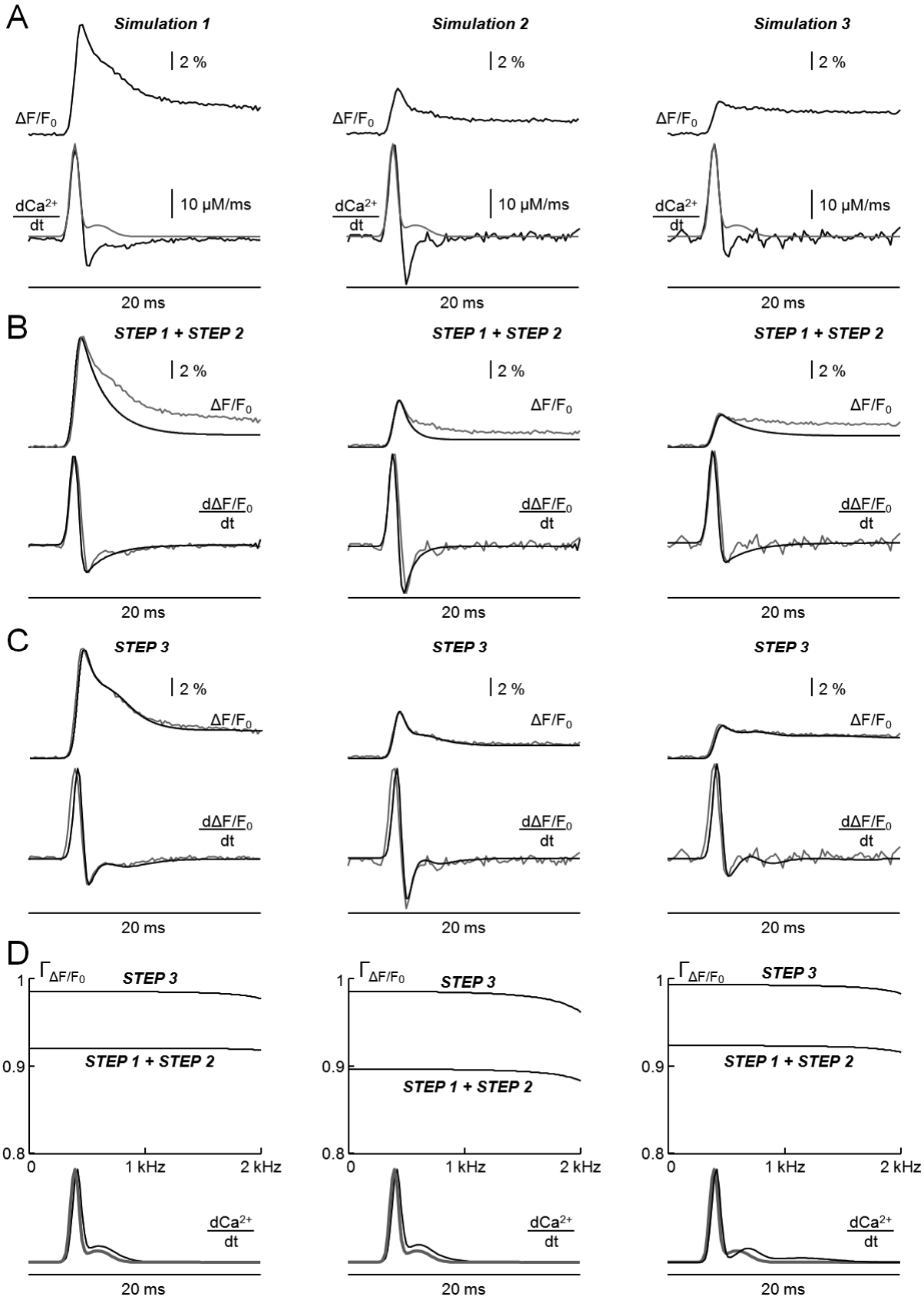

Fig. 4. *Assessment of the protocol from simulated complex cellular scenarios.* (A) Using a model Ca^{2+} current for computer simulations the second current of Fig. 3, the results of 3 computer simulations of OG5N (2 mM) kinetics from complex models with 3 or 4 buffers (see Table 1); the top and bottom black traces are the expected $\Delta F/F_0$ signals and their time derivatives respectively; bottom grey trace is the superimposed current; white noise is added to mimic putative experimental scenarios. (B) Using an input current the single Gaussian function fitting the time derivative rising phase, and optimising the two-buffer parameters of the model (*STEP 1 + STEP 2*), the results of computer simulations (black traces) superimposed to the original signals (grey traces) shown in panel A. (C) With the model parameters established in STEP 2, after optimising the input current (STEP 3), the results of computer simulations (black traces) superimposed to the original signals (grey traces) shown in panel A. (D) Top: $\Gamma_{\Delta F/F0}$, defined in the Materials and Methods, to quantify the similarity of the curves obtained after *STEP 1 + STEP 2* and after *STEP 3*; in all cases, the mean $\Gamma_{\Delta F/F0}$ over 0 – 1 kHz increases to > 0.96 after *STEP* 3. Bottom: the obtained Ca^{2+} currents (black traces) normalised to the peak and superimposed to the original currents.

	Conc. Buffer 1 (μM) K_{on} = 570· μM^{-1}s^{-1} K_D = 10 μM	Conc. Buffer 2 (μM) K_{on} = 570· μM^{-1}s^{-1} K_D = 1 μM	Conc. Buffer 3 (μM) K_{on} = 400· μM^{-1}s^{-1} K_D = 0.4 μM	Conc. Buffer 4 (μM) K_{on} = 200· μM^{-1}s^{-1} K_D = 0.1 μM
Simulation 1	250	0	100	100
Simulation 2	1000	0	500	50
Simulation 3	2000	400	100	20

Table 1. Values of the parameters of the four buffers used in the three simulations of Fig. 4.

In this scenario, fast buffering is small and most of the Ca^{2+} is sequestrated by the slow high-affinity buffer. In the second scenario, the model contains 1 mM of the low-affinity buffer, 500 μM of the fast high-affinity buffer and only 50 μM of the slow high-affinity buffer. In this case, fast buffering is more prominent and later buffering more rapid. Finally, in the third scenario, the model contains 2000 μM of the low-affinity buffer, 400 μM of the medium-affinity buffer, 100 μM of the fast high-affinity buffer and 20 μM of the slow high-affinity buffer. In this last scenario, faster buffering is prevailing with respect to slow buffering. To generate the three $\Delta F/F_0$ signals, we used the same two-component current of the previous paragraph. We added white noise to these curves to mimic experimental scenarios. The $\Delta F/F_0$ signals are reported in Fig. 4(A) (top). The peak of the $\Delta F/F_0$ signal varies in the three cases and it is larger in the first scenario, where fast buffering is weaker. The slope of the faster component of the decay depends on the quantity and speed of the high-affinity buffers. As shown by the time derivatives of the $\Delta F/F_0$ signal reported below (grey traces), the negative peak of the curve, relative to the positive peak, is larger in the second scenario where high-affinity buffering is strong, with respect to low-affinity buffering, but relatively rapid. The slower component of $\Delta F/F_0$ signal decay, after the end of the current, depends on the speed and on the amount of the high-affinity buffers and it is slower in the first scenario. Finally, in the third scenario involving the intermediate (fast) buffer, the time derivative of the $\Delta F/F_0$ signal has a small negative component and it approaches the fast Gaussian component of the current while the slow component is lost (see the right traces in Fig. 4(A)). In the development of a generalised method to estimate the Ca^{2+} current kinetics, the idea is not to precisely predict the kinetics of Ca^{2+} buffering, but to correct for the distortion in the $\Delta F/F_0$ time derivative due to Ca^{2+} sequestration from the indicator. As shown in Fig. 4(A), the time derivative of the $\Delta F/F_0$ signal is always matching the rising phase of the current. Therefore, "*STEP 1*"of the protocol is the fit of the rising phase of the $\Delta F/F_0$ time derivative with one Gaussian function. This curve can be considered the first approximation of the current kinetics to be used in "*STEP 2*"of the protocol. Given this current, the ratio between the positive and the negative peak of the $\Delta F/F_0$ time derivative and the slower decay phase of the signal are two independent conditions that depend on the ratio between the low-affinity (fast) buffer and the high-affinity (slow) buffer, and on the speed of the high-affinity buffer. The positive/negative peak ratio, however, also depends on the slower components of the current and it is expected that the protocol will be less effective when this negative component is small, like in the case of the third scenario in Fig.4(A). By using a simple model with 1 mM of a low-affinity buffer (K_{ON} = 570 μM^{-1}s^{-1} and K_D = 10 μM) and a high-affinity buffer of K_D = 0.2 with K_{ON} = varying from 100 to 570 μM^{-1}s^{-1} and concentration varying from 0 to 500 μM, the two variables can be determined by matching the ratio between the positive and the negative peak of the $\Delta F/F_0$ time derivative and the slower decay phases of

the signal obtained experimentally and by computer simulation. If the experimental ratio is still larger than that obtained by computer simulation, the concentration of the low-affinity buffer is decreased until a match is obtained. Once the "optimal" simple model is obtained in *STEP 2*, the current input is optimised by adding three additional Gaussian components to optimise the match between the experimental and the expected $\Delta F/F_0$ signal in *STEP 3*. At this stage, the parameter of the model can be refined, with corrections of up to ~20% from their original values, to optimise the curve. The optimisation process can go on to maximally increase the mean magnitude squared coherence and it is considered satisfactory if the similarity between the $\Delta F/F_0$ signal and the optimised curve, quantified by the $\Gamma_{\Delta F/F0}$ averaged over the range 0-1 kHz, is >0.96 (see Materials and Methods for details).

The results of applying this semi-automatic protocol to the three scenarios of Fig. 4(A) are shown in Fig. 4(B-C). In Fig. 4(B), the expected $\Delta F/F_0$ signal and its time derivative, produced by a single fast Gaussian input (*STEP 1*) with the "optimal" simple parameters of the model (*STEP 2*), are plotted and superimposed to the corresponding traces of the real $\Delta F/F_0$ signal. Remarkably, but as expected from the previous observations, the $\Delta F/F_0$ time derivatives are similar despite the signals are substantially different. In Fig. 4(C), the expected $\Delta F/F_0$ signal and its time derivative, produced after correcting the input with three additional Gaussian components (*STEP 3*), are again plotted and superimposed to the corresponding traces of the real $\Delta F/F_0$ signal. This correction, performed to improve the similarity between the experimental and simulated signals, increased the mean $\Gamma_{\Delta F/F0}$ at 0-1 kHz from ~0.9 to >0.98 in all three cases as shown in Fig. 4(D). In all three scenarios, a slower current component was necessary to match the experimental $\Delta F/F_0$ signal. In the first two scenarios, where the $\Delta F/F_0$ time derivative negative component is large, the slow component of the current obtained with the protocol was only ~20% larger and delayed by a few hundred microseconds with respect to the real one.

The current obtained by applying our protocol is not a faithful reproduction of the real current, but can be considered a satisfactory estimate of its kinetics. The protocol performs better in the first two scenarios where the fast negative component of the $\Delta F/F_0$ time derivative is less dependent on the slower component of the current. Thus, the Gaussian function that matches the rising phase of the time derivative allowed the determination of the optimal model parameters since the negative component of the $\Delta F/F_0$ time derivative depended only weakly on the slower current component. In contrast, in the third scenario, the smaller negative component of the $\Delta F/F_0$ time derivative depended more strongly on the slow component of the current affecting the determination of the model parameters from the fast component of the current. In the previous method applicable to CA1 hippocampal pyramidal neurons, it was convenient to oversample signals at 20 kHz and then applying a smoothing algorithm to reduce the noise and to obtain a faithful calculation of the time derivative (Jaafari et al., 2014). Here, where the initial estimate of the time derivative is based on the fit of the rising phase with a Gaussian function, applying a filter is less critical and recordings can be done at 5 kHz increasing the number of points sampled. We can, in this way, extrapolate a realistic kinetic curve for the Ca^{2+} current where the fidelity in reproducing the real current depends on how large and fast the negative component of the $\Delta F/F_0$ time derivative is. The proper assessment of this new method required the validation through biological experiments presented in the next two paragraphs.

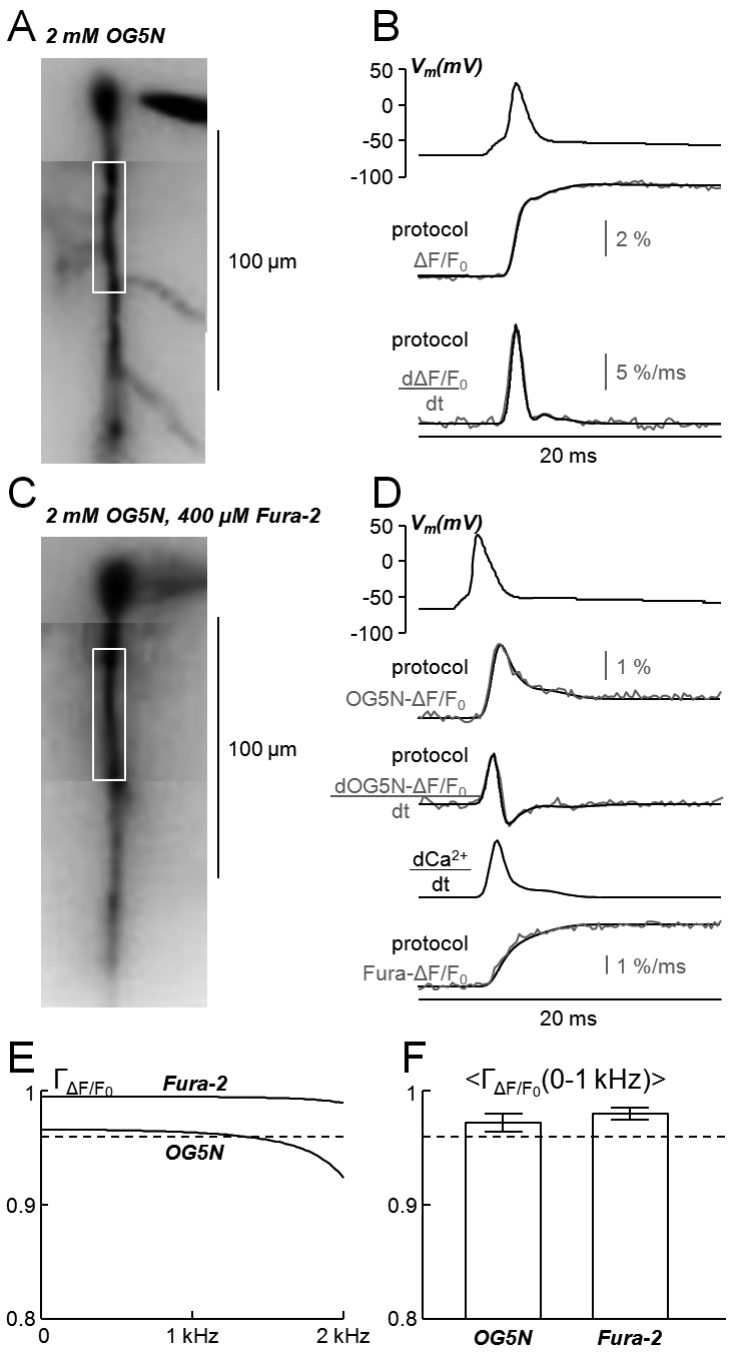

Fig. 5. *Validation of the protocol in CA1 hippocampal pyramidal neurons.* (A) CA1 hippocampal pyramidal neuron filled with 2 mM OG5N with a region of interest indicated. (B) Top trace: action potential. Middle traces: associated OG5N-$\Delta F/F_0$ signal; grey trace is the experiment; black trace is the optimal curve from computer simulation. Bottom traces: the extracted Ca^{2+} current kinetics leading to the optimal curves (black trace) superimposed to the OG5N-$\Delta F/F_0$ time derivative (grey trace).(C) CA1 hippocampal pyramidal neuron filled with 2 mM OG5N and 400 µM Fura-2 with a region of interest indicated. (D) From the top, 1st trace: action potential. From the top, 2nd and 3rd traces: associated OG5N-$\Delta F/F_0$ signal and its time derivative in the region of interest; grey traces are the experiments; black traces are the optimal curves from computer simulation. From the top, 4th trace: the extracted Ca^{2+} current kinetics leading to the optimal curves. From the top, 5th traces: the associated Fura-$\Delta F/F_0$ signal in the region of interest; grey trace is the experiment; black trace is the curve from computer simulation. (C) $\Gamma_{\Delta F/F0}$ calculated for both the OG5N-$\Delta F/F_0$ signal and the Fura-$\Delta F/F_0$ signal reported in panel B. (D) Mean ± SD of the mean $\Gamma_{\Delta F/F0}$ ($<\Gamma_{\Delta F/F0}>$) averaged over 0 – 1 kHz from five cells for OG5N-$\Delta F/F_0$ signals and Fura-$\Delta F/F_0$ signals. In C and D, the dotted lines indicate the 0.96 minimal value of $<\Gamma_{\Delta F/F0}>$ for the experimental and simulated curves to be similar. All data were from averages of 16 trials.

3.3 Experimental validation of the protocol in CA1 hippocampal pyramidal neurons

The dendrites of CA1 hippocampal pyramidal neurons do not have any slow endogenous buffer that significantly affects the fast OG5N-$\Delta F/F_0$ kinetics (Jaafari et al., 2014). Therefore, as shown in the example cell of Fig. 5(A), the OG5N-$\Delta F/F_0$ signal associated with an action potential (Fig. 5(B), top trace) had slope equal to zero after the end of its rising phase (Fig. 5(B), middle trace). When applying *STEP 2* of our protocol to this signal, the optimal concentration of the slow buffer was obviously zero and the multivariate Gaussian function optimised on the OG5N-$\Delta F/F_0$ signal matched the OG5N-$\Delta F/F_0$ time derivative (Fig. 5(B), bottom traces). If we add to the internal solution 400 µM Fura-2, i.e. an exogenous buffer of known kinetics (K_{ON} = 570 $\mu M^{-1}s^{-1}$ as in Canepari and Mammano, 1999 and K_D = 0.24 µM at 33 ºC as in Shuttleworth and Thompson, 1991), the OG5N-$\Delta F/F_0$ signal is artificially changed by the slower binding to Fura-2 that can be directly measured since this indicator is excited at a different wavelength (385 nm) with respect to OG5N (470 nm). Therefore, the match of the Fura-$\Delta F/F_0$ signal with the time course of the slow buffer in the model can be used to validate the protocol as predictor of the real current. In the cell of Fig. 5(C), filled with 400 µM Fura-2, the OG5N-$\Delta F/F_0$

signal associated with an action potential (Fig. 5(D), top two traces) had negative slope (Fig. 5(D), third trace from the top). The OG5N-$\Delta F/F_0$ signal and its time derivative were used to set the optimal parameters in the model and the current that matched the experimental traces (Fig. 5(D), fourth trace from the top), as described in the previous paragraph. As expected, the optimal concentration of the slow buffer was ~400 µM, i.e. the concentration of Fura-2 in the pipette. The time course of the bound slow buffer from the computer simulation was then superimposed to the measured Fura-$\Delta F/F_0$ signal (Fig. 5(D), bottom traces). The two curves had the same kinetics. In this particular cell, the mean $\Gamma_{\Delta F/F0}$ at 0-1 kHz ($<\Gamma_{\Delta F/F0}>$) was 0.97 for the OG5N-$\Delta F/F_0$ signal and>0.98 for the Fura-$\Delta F/F_0$ signal (Fig. 5(E)). The same experiment was performed in five cells altogether, always obtaining a satisfactory similarity between the experimental and the simulated curve for both indicators. Hence, in N = 5 cells, $<\Gamma_{\Delta F/F0}>$ was 0.972 ± 0.008 for OG5N and 0.990 ± 0.005 for Fura-2 (Fig. 5(F)). The experimental validation of the method in CA1 hippocampal pyramidal neurons was meaningful since, in this cell, the slow buffering was artificially caused by a single relatively simple buffer (Fura-2) with known characteristics. The fact that CA1 hippocampal pyramidal neurons have negligible slow buffers may however explain why the protocol was efficient in finding a Ca^{2+} current producing signals that matched the $\Delta F/F_0$ signal of both indicators. Next, we report the same type of experimental validation in PNs where slow buffering is naturally produced by multiple proteins with more complex kinetics.

3.4 Experimental validation of the protocol in cerebellar Purkinje neurons

In contrast to CA1 hippocampal pyramidal neurons, the negative slope of OG5N-$\Delta F/F_0$ signals is due to complex binding to several proteins that cannot be directly monitored. Nevertheless, Fura-2 can be added to the internal solution and its binding to Ca^{2+} can be monitored to assess whether our protocol finds a current for which a satisfactory match between the experimental $\Delta F/F_0$ signals and the simulated curves can be found. This experiment would provide a validation that the method works also in more complex experimental scenarios. The cell of Fig. 6(A) was filled with 400 µM Fura-2 and 2 mM OG5N. In this set of analysis, the model included Fura-2 as fixed buffer at concentration of 400 µM, K_{ON} = 570 $\mu M^{-1}s^{-1}$ and K_D = 0.24 µM. The optimisation of the parameters of the endogenous buffer (*STEP 2*) was performed exclusively on the OG5N-$\Delta F/F_0$ signal and its time derivative, as in the previous cases. The fast Ca^{2+} transient was associated with an evoked climbing fibre EPSP (Fig. 6(B), top trace). The time course of the OG5N-$\Delta F/F_0$ signal was biphasic (Fig. 6(B), second traces from the top), but the time derivative had still a fast negative peak (Fig. 6(B), third traces from the top). The experimental traces were matched by the curves obtained with protocol where the input current had a fast and a slow distinct component (Fig. 6(B), fourth trace from the top). Remarkably, the kinetics of the expected Ca^{2+} bound to Fura-2 matches, as in the case of CA1 hippocampal pyramidal neurons, the time course of the Fura-$\Delta F/F_0$ signal (Fig. 6(B), bottom traces). In this particular cell,$<\Gamma_{\Delta F/F0}>$ was 0.98 for the OG5N-$\Delta F/F_0$ signal and>0.99 for the Fura-$\Delta F/F_0$ signal (Fig. 6(C)). The same experiment was performed in six cells altogether, always obtaining an excellent match between the experimental and the simulated curve for both indicators. In N = 6 cells, $<\Gamma_{\Delta F/F0}>$ was 0.985 ± 0.004 for OG5N and 0.993 ± 0.005 for Fura-2 (Fig. 6(D)). We concluded that our protocol is also capable of reproducing the time course on both OG5N-$\Delta F/F_0$and Fura-$\Delta F/F_0$ signals in

PNs, suggesting that the generating Ca^{2+} current input is kinetically a realistic approximation of the real current associated with the climbing fibre EPSP.

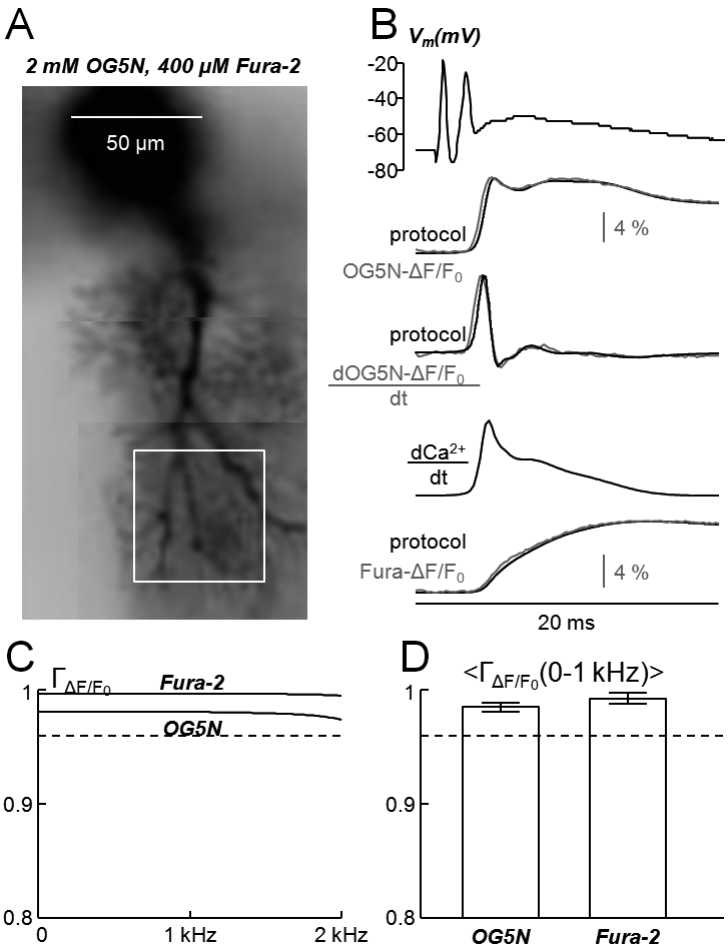

Fig. 6. *Validation of the protocol in PNs.* (A) PN filled with 2 mM OG5N and 400 µM Fura-2 with a dendritic region of interest indicated. (B) From the top, 1st trace: climbing fibre EPSP. From the top, 2nd and 3rd traces: the associated OG5N-$\Delta F/F_0$ signal and its time derivative in the region of interest; grey traces are the experiments; black traces are the optimal curves from computer simulation. From the top, 4th trace: the extracted Ca^{2+} current kinetics leading to the optimal curves. From the top, 5th traces: the associated Fura-$\Delta F/F_0$ signal in the region of interest; grey trace is the experiment; black trace is the curve from computer simulation. (C) $\Gamma_{\Delta F/F0}$ calculated for both the OG5N-$\Delta F/F_0$ signal and the Fura-$\Delta F/F_0$ signal reported in panel B. (D) Mean ± SD of $<\Gamma_{\Delta F/F0}>$ from six cells for OG5N-$\Delta F/F_0$ signals and Fura-$\Delta F/F_0$ signals. In C and D, the dotted lines indicate the 0.96 minimal value of $<\Gamma_{\Delta F/F0}>$ for the experimental and simulated curves to be similar. All data were from averages of 9 trials.

3.5 Measurement of Ca^{2+} current kinetics in cerebellar Purkinje neurons

In the previous paragraphs, our novel method to extract the Ca^{2+} current kinetics from OG5N-$\Delta F/F_0$ signals was first assessed using simulated artificial scenarios and then validated in CA1 hippocampal pyramidal neurons and PNs using combined fluorescence measurements of the added exogenous buffer Fura-2. In this last paragraph of the Results, we eventually report the first measurements of physiological Ca^{2+} currents associated with climbing fibre EPSPs in PNs using our new protocol. In the cell of Fig. 7(A), filled with 2 mM OG5N (and no Fura-2), we analysed the $\Delta F/F_0$ signals associated with a climbing fibre EPSP (Fig. 7(B), top traces) in three sample regions indicated on the image. As in all previous cases, in all the three regions the protocol was capable to find realistic currents (Fig. 7(B), bottom traces) that produced optimal curves matching the $\Delta F/F_0$ signal and its time derivative (Fig. 7(B), middle traces).

Notably, although the $\Delta F/F_0$ signals were quite different in the three regions, the optimal match was found using the same parameters of the model, while only the current changed from a region to another. In this experiment, $<\Gamma_{\Delta F/F0}>$ was >0.98 in all three regions. In the cell of Fig. 7(C), we analysed the $\Delta F/F_0$ signals associated with climbing fibre EPSPs elicited at different initial membrane potential (Fig. 7(D), top traces) in a larger region. Interestingly, the $\Delta F/F_0$ signal increased at increasing initial membrane potential and

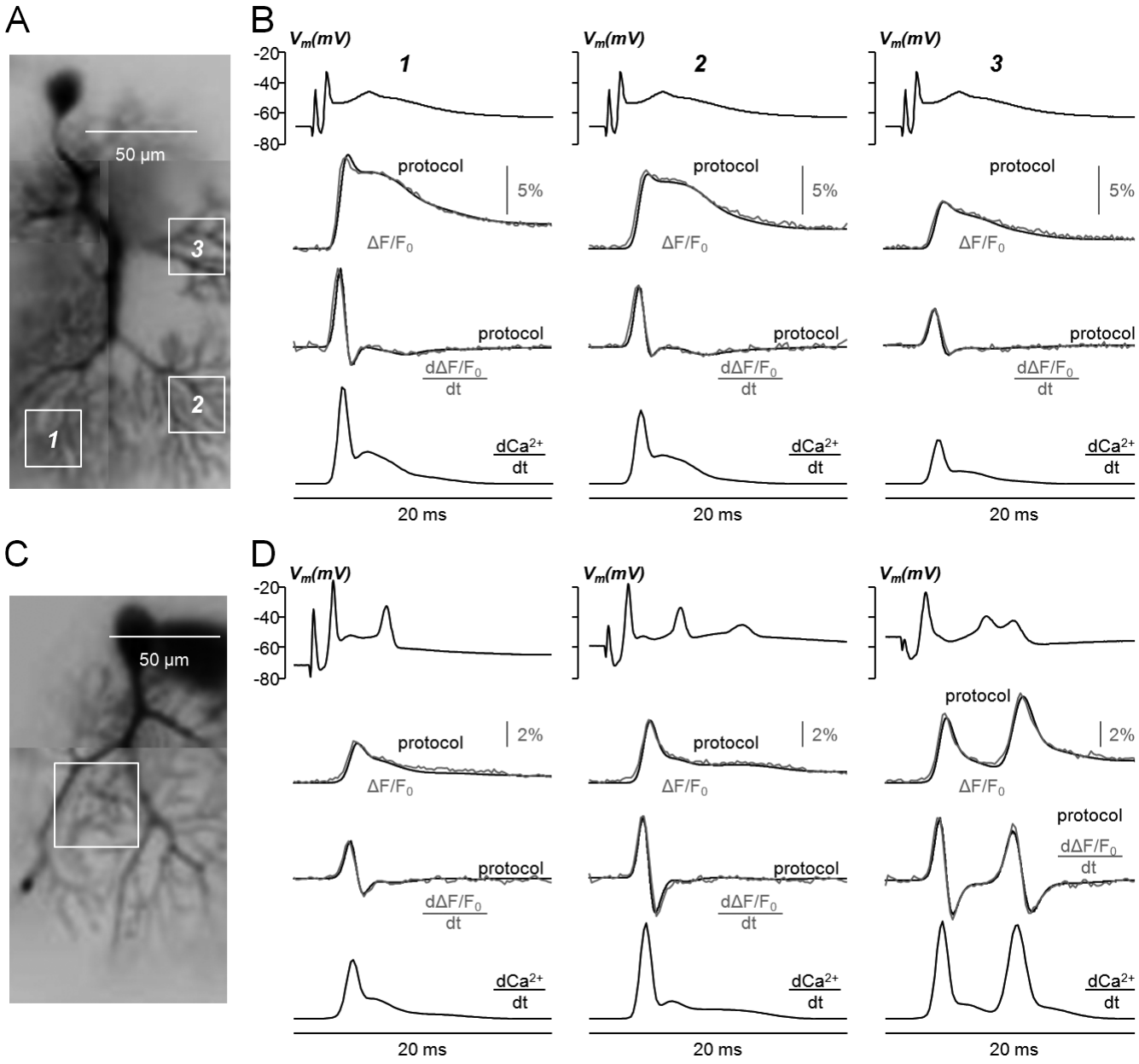

Fig. 7. *Examples of extraction of Ca^{2+} current kinetics in PNs.* (A) PN filled with 2 mM OG5N and three numbered regions of interest indicated. (B) Top traces: a climbing fibre EPSP. Middle traces: the associated OG5N-$\Delta F/F_0$ signals and the time derivatives in the three regions of interest; grey traces are the experimental data; black traces are the optimal curves from computer simulation. Bottom traces: the extracted Ca^{2+} current kinetics leading to the above optimal curves. (C) Another PN filled with 2 mM OG5N and one dendritic region of interest indicated. (D) Top traces: climbing fibre EPSPs at different initial membrane potential. Middle traces: the associated OG5N-$\Delta F/F_0$ signals and the time derivatives in the region of interest; grey traces are the experimental data; black traces are the optimal curves from computer simulation. Bottom traces: the extracted Ca^{2+} current kinetics leading to the above optimal curves. All data were from averages of 4 trials.

exhibited two peaks for the less negative initial membrane potential (Fig. 7(D), middle traces). The protocol was capable to find realistic currents (Fig. 7(D), bottom traces) for the three different cases using, again, only one set of parameters. In this experiment, $<\Gamma_{\Delta F/F0}>$ was >0.97 in all three cases. We performed this analysis in six cells altogether, either focussing of different dendritic regions or at climbing fibre

EPSPs elicited at different initial membrane potentials. The values of the optimal model parameters found in each cell, as well as the averaged $<\Gamma_{\Delta F/F0}>$ values (always > 0.97), are reported in Table 2. From these values, it is possible to estimate the buffer capacity as the summation of the fast and slow buffer concentrations divided by their respective K_Ds. In this group of six cells, this was 2181 ± 282, in agreement with the mean value of 2129 reported by Fierro and Llano in PNs from rats older than 15 days (Fierro and Llano, 1996). Thus, we concluded that the parameters of the model leading to the extraction of the optimal Ca^{2+} current kinetics are consistent with the measured buffer capacity of this cell type.

	Conc. fast Buffer (μM) K_{ON} **= 570· μM^{-1}s^{-1}** K_D **= 10· μM**	**Conc. slow Buffer (μM)** K_D **= 0.2 μM**	**K_{ON} slow Buffer (μM^{-1}s^{-1})**	**$<\Gamma_{\Delta F/F0}>$**
Cell 1	400	400	230	0.987
Cell 2	180	490	300	0.975
Cell 3	680	400	280	0.992
Cell 4	290	350	210	0.988
Cell 5	300	500	260	0.974
Cell 6	500	430	200	0.994

Table 2. Values of the model parameters obtained by analysing OG5N-$\Delta F/F_0$ signals associated with climbing fibre EPSPs in six cells. The first two cells are those of Fig. 7.

3. Discussion

In this article, we presented a novel strategy to extrapolate the kinetics of Ca^{2+} currents from fluorescence Ca^{2+} measurements using OG5N, or other low-affinity indicators, in cases where the method based on the simple calculation of the time derivative fails. A low-affinity Ca^{2+} indicator, which equilibrates in less than 200 μs, has the intrinsic ability of tracking fast neuronal Ca^{2+} currents. In many cases, the time course of the Ca^{2+} current is matched by the time derivative of the fractional change of fluorescence (Sabatini and Regehr, 1998; Jaafari et al., 2014). This method fails when Ca^{2+} unbinds from the indicator over a time scale that is longer than the current duration, but sufficiently short to distort the estimate of Ca^{2+} influx dynamics by fluorescence measurement. In other words, this method fails when the $\Delta F/F_0$ signal decays rapidly generating a negative component in its time derivative.

The Ca^{2+} sequestration responsible for the rapid decay of the $\Delta F/F_0$ signal is due, in reality, to what we define “slow buffer”, where slow is referred to the faster buffer equilibrating over a time scale shorter than the current duration and similar to the equilibration time of low-affinity indicators. In cells, slow buffers typically correspond to calcium binding proteins such as Calmodulin (Faas et al., 2011), Calretinin (Faas et al., 2007), Parvalbumin (Lee et al., 2000) and Calbindin (Nägerl et al., 2000). In the case of PNs, the fast decay time of the OG5N-$\Delta F/F_0$ signal, preventing the measurement of the Ca^{2+} current, is due to Calbindin-D28k (Airaksinen et al., 1997) and Parvalbumin (Schmidt et al., 2003). Modelling the kinetics of a Ca^{2+} transient is a complex task since Calbindin-D28k and Parvalbumin have multiple binding sites with different kinetic parameters (Schmidt and Eilers, 2009; Canepari and Vogt, 2008) and the diffusion of

these Ca^{2+} binding proteins also plays an important role (Schmidt et al., 2012). Thus, the extraction of the precise Ca^{2+} current kinetics is limited by the absence of detailed information on slow buffering that is different from cell to cell and, in general, from site to site in the same cell. While the effect of diffusion can be neglected in recordings from relatively large dendritic portions, like in this case, our method is based on a simplified model with only one slow buffer and three free parameters. Reducing the degrees of freedom to three allowed the development of a semi-automatic protocol in which the optimisation of the model parameters and of the current kinetics, leading to the fit of the OG5N-$\Delta F/F_0$ signal, is done in two distinct steps. The condition permitting the separation between the model parameters setting and the current reconstruction is that the fast rising phase of the current can be reliably approximated with the time derivative of the OG5N-$\Delta F/F_0$ signal. The consistency of the curve obtained with this protocol in reproducing the kinetics of the real buffering depends on the characteristics of the buffer and of the current. In the cases of the first two simulations in Fig. 4, or in the case of PNs (Fig. 7), the model parameters can be reliably obtained from the fast current component (i.e. the initial OG5N-$\Delta F/F_0$ time derivative) and the method extracts a curve that approaches the kinetics of the Ca^{2+} current, also for the slower components. In the putative case of a buffer with intermediate behaviour between a “fast” and a “slow” buffer, (see the third simulation in Fig. 4), the analysis of the time course of the OG5N-$\Delta F/F_0$ signal is more complicated and may lead to unreliable determination of the model parameter and a more distorted estimation of the current kinetics. This observation points out the limits of this method, which, in contrast to the straightforward time derivative method, can only produce an estimate and not a direct measurement of the Ca^{2+} current kinetics. Yet, the information extracted by this curve is very important. The extrapolation of diverse current components may be associated to the activation and de-activation of different type of HVA-VGCCs and LVA-VGCCs (see as an example Jaafari and Canepari, 2016). In the dendrites of PNs, for instance, the fast and the slow component of the Ca^{2+} current associated with a climbing fibre EPSP (Fig. 7) are likely associated with the activation of P/Q-type VGCCs (Usowitz et al., 1992) and T-type Ca^{2+} channels (Isope et al., 2012). Thus, the extrapolation of a curve that approaches the kinetics of the Ca^{2+} current can be used to quantitatively investigate the variability of channels activation at different dendritic sites, the modulation of channel activation due to physiological activity or to pharmacological action or the variability in channel activation in different animals (for instance during development).

The ability to perform the measurement of fast Ca^{2+} currents relies on the recent availability of cameras capable of acquiring frames, at relatively high spatial resolution and sensitivity, in the kHz range (Davies et al., 2013). If the $\Delta F/F_0$ signal is recorded for a longer period (> 200 ms), its kinetics is dominated, over this time scale, by a slower decay time due to Ca^{2+} extrusion (see for instance Majewska et al., 2000). We included Ca^{2+} extrusion in our model with simple Michaelis-Menten kinetics. As shown in Fig. 3, Ca^{2+} extrusion does not affect the OG5N-$\Delta F/F_0$ time derivative associated with a fast Ca^{2+} transient. We can however imagine measuring $\Delta F/F_0$ signals associated with currents with a duration that is longer than the equilibration time of the slow buffer. In this case, this buffer behaves as a fast buffer, but there will be a negative component of the $\Delta F/F_0$ time derivative due to Ca^{2+} extrusion. Under this condition, the method presented in this article can be modified by considering only one “fast” buffer and by

optimising the parameters of Ca^{2+} extrusion on the $\Delta F/F_0$ signal to extrapolate the Ca^{2+} current. Thus, the approach we developed can be considered a generalised method to estimate the full kinetics of all types of physiological Ca^{2+} currents.

Conflict of interest statement

The authors have no conflict of interest to disclose.

Acknowledment

This work was supported by the *Agence Nationale de la Recherche* through three grants: 1. Grant *WaveFrontImag*, program number ANR-14-CE17-0006-01; 2. Labex *Ion Channels Science and Therapeutics*, program number ANR-11-LABX-0015; 3. National Infrastructure France Life Imaging "Noeud Grenoblois" ; and by the *Federation pour la recherché sur le Cerveau* (FRC) through the grant *Espoir en tête* (in partnership with Rotary France). We thank Joseph Gallagher and Bertrand Fourcade for reading the manuscript before submission.

REFERENCES

Airaksinen MS, Eilers J, Garaschuk O, Thoenen H, Konnerth A, Meyer M. Ataxia and altered dendritic calcium signalling in mice carrying a targeted nullmutation of the calbindin D28k gene. Proc Natl Acad Sci USA 1997; 94:1488-93.

Canepari M, Mammano F. Imaging neuronal calcium fluorescence at high spatio-temporal resolution. J. Neurosci. Methods 1999; 87:1 -11.

Canepari M, Odgen D. Kinetic, pharmacological and activity-dependent separation of two Ca^{2+} signalling pathways mediated by type 1 metabotropic glutamate receptors in rat Purkinje neurons. J Physiol 2006; 573:65-82.

Canepari M, Vogt, KE. Dendritic Spike Saturation of Endogenous Calcium Buffer and Induction of Postsynaptic Cerebellar LTP. PLoS ONE 2008; 3:e4011.

Canepari M, Vogt K, Zecevic D. Combining voltage and calcium imaging from neuronal dendrites. Cell Mol Neurobiol 2008; 58: 1079-93.

Canepari M, Willadt S, Zecevic D, Vogt KE. Imaging Inhibitory Synaptic Potentials Using Voltage Sensitive Dyes. Biophys J 2010; 2032-40.

Davies R, Graham J, Canepari M. Light sources and cameras for standard in vitro membrane potential and high-speed ion imaging. J Microsc 2013; 251:5-13.

Faas GC, Mody I. Measuring the kinetics of calcium binding proteins with flash photolysis. Biochim Biophys Acta 2012; 1820:1195-204.

Faas GC, Raghavachari S, Lisman JE, Mody I. Calmodulin as a direct detector of Ca2+ signals. Nat Neurosci 2011; 14:301-4.

Faas GC, Schwaller B, Vergara JL, Mody I. Resolving the fast kinetics of cooperative binding: Ca2+ buffering by calretinin. PLoS Biol 2007; 5:e311.

Fierro L, Llano I. High endogenous calcium buffering in Purkinje cells from rat cerebellar slices. J Physiol 1996; 496:617-25.

Helmchen F, Imoto K, Sakmann B. 1996. Ca2+ buffering and action potential-evoked Ca2+ signaling in dendrites of pyramidal neurons. Biophys J 1996; 70:1069 –1081.

Isope P, Hildebrand ME, Snutch TP. Contributions of T-type voltage-gated calcium channels to postsynaptic calcium signaling within Purkinje neurons. Cerebellum 2012;11:651-65.

Jaafari N, Canepari M. Functional coupling of diverse voltage-gated Ca(2+) channels underlies high fidelity of fast dendritic Ca(2+) signals during burst firing. J Physiol 2016; 549:967-83.

Jaafari N, De Waard M, Canepari M. Imaging Fast Calcium Currents beyond the Limitations of Electrode Techniques. Biophys J 2014; 107:1280-88.

Jaafari N, Marret E, Canepari M. Using simultaneous voltage and calcium imaging to study fast Ca2+ channels. Neurophotonics 2015; 2:021010.

Kao JP, Tsien RY. Ca2+ binding kinetics of fura-2 and azo-1 from temperature-jump relaxation measurements. Biophys J 1988 ; 53:635-39.

Lee SH, Schwaller B, Neher E. Kinetics of Ca2+ binding to parvalbumin in bovine chromaffin cells: implications for [Ca2+] transients of neuronal dendrites. J Physiol 2000; 525:419-32.

Majewska A, Brown E, Ross J, Yuste R. Mechanisms of calcium decay kinetics in hippocampal spines: role of spine calcium pumps and calcium diffusion through the spine neck in biochemical compartmentalization. J Neurosci 2000; 20:1722-34.

Maravall M, Mainen ZF, Sabatini BL, Svoboda K. Estimating intracellular calcium concentrations and buffering without wavelength ratioing. Biophys J 200 ; 78:2655-67.

Miyakawa H, Lev-Ram V, Lasser-Ross N, Ross WN. Calcium transients evoked by climbing fiber and parallel fiber synaptic inputs in guinea pig cerebellar Purkinje neurons. J Neurophysiol 1992; 68:1178-89.

Nägerl UV, Novo D, Mody I, Vergara JL. Binding kinetics of calbindin-D(28k) determined by flash photolysis of caged Ca(2+). Biophys J 2000; 79:3009-18.

Nowycky MC, Pinter MJ. Time courses of calcium and calcium-bound buffers following calcium influx in a model cell. Biophys J 1993; 64:77-91.

Oppenheim AV, Schafer RW. Discrete-Time Signal Processing, Upper Saddle River, NJ: Prentice-Hall; 1999.

Pethig R, Kuhn M, Payne R, Adler E, Chen TH, Jaffe LF. On the dissociation constants of BAPTA-type calcium buffers. Cell Calcium 1989; 10: 491-8.

Sabatini BL, Regehr WG. Optical measurement of presynaptic calcium currents. Biophys J 1998; 74:1549-63.

Schmidt H, Arendt O, Eilers J. Diffusion and extrusion shape standing calcium gradients during ongoing parallel fiber activity in dendrites of Purkinje neurons. Cerebellum 2012; 11:694-705.

Schmidt H, Eilers J. Spine neck geometry determines spino-dendritic cross-talk in the presence of mobile endogenous calcium binding proteins. J Comput Neurosci 2009; 27:229-43.

Schmidt H, Stiefel KM, Racay P, Schwaller B, Eilers J. Mutational analysis of dendritic Ca2+ kinetics in rodent Purkinje cells: role of parvalbumin and calbindin D28k. J Physiol 2003; 551:13-32.

Shuttleworth TJ, Thompson JL. Effect of temperature on receptor-activated changes in [Ca2+]i and their determination using fluorescent probes. J Biol Chem 1991; 266:1410-4.

Usowicz MM, Sugimori M, Cherksey B, Llinás R. P-type calcium channels in the somata and dendrites of adult cerebellar Purkinje cells. Neuron 1992; 9:1185-99.

Vogt KE, Gerharz S, Graham J, Canepari M. High-resolution simultaneous voltage and Ca^{2+} imaging. J Physiol 2011a; 589:489-94.

Vogt KE, Gerharz S, Graham J, Canepari M. Combining membrane potential imaging with L-glutamate or GABA photorelease. PLoS ONE 2011b; 6:e24911.

Welch PD. The Use of Fast Fourier Transform for the Estimation of Power Spectra: A Method Based on Time Averaging Over Short, Modified Periodograms. IEEE Trans. Audio Electroacoust 1967; AU-15: 70-3.